Post-embryonic development and aging of the appendicular skeleton in *Ambystoma mexicanum*

Camilo Riquelme-Guzmán[1], Maritta Schuez[1], Alexander Böhm[1], Dunja Knapp[1], Martina Rauner[2,3], Tatiana Sandoval-Guzmán[1,3]

[1]Technische Universität Dresden, CRTD/ Center for Regenerative Therapies TU Dresden, Dresden, Germany

[2]Department of Medicine III, Universitätsklinikum Dresden, Dresden, Germany.

[3]Center for Healthy Aging, Universitätsklinikum Dresden, Dresden, Germany.

Correspondence

Tatiana Sandoval-Guzmán, Technische Universität Dresden, CRTD/Center for Regenerative Therapies TU Dresden, Dresden Germany

Email: tatiana.sandoval_guzman@tu-dresden.de

Keywords

Axolotl, ossification, aging, chondrocytes, osteoblasts

Abstract

Background

The axolotl is a key model organism for studying appendicular regeneration in vertebrates. The axolotl limb complexity resembles that of humans in structure and tissue components; however, axolotl limbs develop post-embryonically. In this work, we evaluated the post-embryonic development of the appendicular skeleton and its changes with aging.

Results

Juvenile skeletal elements are formed mostly by $SOX9^+/COL1A2^+$ cartilage cells. Ossification of the appendicular skeleton starts when animals reach a total length of 10 cm, and cartilage cells are replaced by a primary ossification center, consisting of cortical bone and an adipocyte-filled marrow cavity. Vascularization is associated to the ossification center and to the formation of the marrow cavity. We identified the contribution of *Col1a2*$^+$ cells to bone and adipocytes. Moreover, ossification progresses with age towards the epiphyses of long bones. Even though axolotls are neotenic salamanders, ossification remains responsive to L-thyroxine, increasing the rate of bone formation.

Conclusions

Bone maturation is a continuous process in axolotls that extends throughout the life span of the axolotls. Ossification of the appendicular bones is slow and continues until the complete element is ossified. The cellular components of the appendicular skeleton change accordingly during ossification, creating a heterogenous landscape in each element.

Introduction

The axolotl (*Ambystoma mexicanum*) is a gold standard for studying limb regeneration in vertebrates. The progenitor cells in the blastema, a key structure for epimorphic regeneration, are a heterogeneous population that remains restricted to their embryonic origin (Kragl et al., 2009). Given the cellular heterogeneity of the blastema, the contribution of specific cell populations during regeneration has been the focus of significant research in the last decade. An interesting exception is the skeleton: cells embedded in the skeletal matrix do not participate in regeneration, instead, the skeleton is restored by periskeletal cells and dermal fibroblasts (Currie et al., 2016; Gerber et al., 2018; McCusker et al., 2016).

While mammals are born with ossified bones, ossification in most amphibians is coupled with metamorphosis (Miura et al., 2008; Quilhac et al., 2014; Rozenblut and Ogielska, 2005). However, axolotls remain neotenic and, hence, they maintain juvenile features throughout life and only rarely undergoing metamorphosis. Their adulthood is marked by reaching sexual maturity, slowing growth rate and by ossification of the appendicular skeleton (Malacinski, 1978; Vieira et al., 2019). The physiological context in which appendicular ossification occurs in axolotl as well as the cellular transitions within the skeleton are unclear. In the anuran amphibium, *Xenopus laevis*, the extent of ossification negatively correlates with the regenerative potential of the limb. During metamorphosis and as bone ossifies, regeneration declines in the ossifying areas, while amputation at the cartilaginous joints still regenerates (Wolfe et al., 2000). Limb regeneration in salamanders remains a feature of adult animals; however, regeneration also declines with age and after metamorphosis (Monaghan et al., 2014). It remains unclear if the correlation between appendicular ossification and decreased regeneration holds true for the axolotl, but more importantly, if the regeneration mechanisms studied so far are replicated when the cellular and matrix landscape changes in the skeleton. In this study, we analyzed larvae, adult and aged axolotls to document the transition of the appendicular skeleton from cartilaginous to ossified skeleton.

In general, appendicular bones develop by endochondral ossification, a process where a cartilage anlage is replaced by bone (reviewed in (Kozhemyakina et al., 2015; Olsen et al., 2000)). During development, mesenchymal progenitors condensate and form a cartilage primordium which expands by proliferation of chondrocytes. Cells located in the central diaphysis differentiate into hypertrophic chondrocytes (HCs), which subsequently induce the

96 recruitment of blood vessels, osteoclasts and osteoblasts, giving rise to the primary
97 ossification center. Within the diaphysis, the cartilage matrix is degraded, osteoblasts replace
98 the tissue with cortical bone and a marrow cavity is formed. Simultaneously, osteoblasts
99 located in the perichondrium form a bone collar around the diaphysis and the periosteum is
100 established. Many HCs undergo apoptosis during endochondral ossification; however, several
101 studies have shown a partial contribution from HCs to bone formation through
102 transdifferentiation into osteoblasts (Giovannone et al., 2019; Jing et al., 2017; Yang et al.,
103 2014). Moreover, Giovannone *et al* showed that HCs can also transdifferentiate into
104 adipocytes in the ceratohyal bone in zebrafish, highlighting the importance and participation
105 of HCs in the ossification process. In axolotl, however, endochondral ossification is a post-
106 embryonic process. If it is driven by the hormonal changes of sexual maturity, environmental
107 cues or body mass, is not yet determined.

108 In this work, we evaluated the post-embryonic development of the appendicular
109 skeleton of axolotls, from larvae to aged adults. We analyzed the morphological and cellular
110 changes in the zeugopodial elements, the radius and ulna, and we identified the timing in
111 which ossification of those elements occurred. Moreover, we examined the cellular landscape
112 of radius and the possible contribution of chondrocytes to bone formation in ulnas. Finally,
113 we observed in aged animals (5- to 20-years) a continuous ossification in all limb skeletal
114 elements. Hence, our work provides a detailed view of how the appendicular skeleton,
115 particularly the zeugopod, matures from a cartilage anlage towards a bone. Urodeles are the
116 only vertebrates with the ability to regenerate a whole limb as adults, therefore they offer the
117 unique opportunity to gain important insights to advance regenerative medicine.
118
119
120
121
122
123
124
125
126
127

Results

The appendicular skeleton is progressively ossified with growth

Few studies on aged animals beyond the well-determined larval stages (Schreckenberg and Jacobson, 1975) and the neoteny of the axolotl, raises controversy on the limit of its growth. In this study, we used animals grown in fully standardized conditions (Khattak et al., 2014) and we defined their appendicular development in relation to their maturation stage. We created a growth chart (normogram) and observed a correlation between size and age for both total length (TL) and snout to vent length (SV) (Fig. 1A, B). Both measurements presented a similar trend: a rapid growth phase in the first 24 months of age followed by a stationary phase. We documented the growth in the context of sexual maturity in our axolotl colony. The first signs of secondary sexual features in males appear around 10 months of age, and by 12 months these features are fully developed. However, a successful mating starts only between 11 and 12 months of age. Females develop the first secondary sexual features slightly later than males (between 10-11 months of age) but like males, by 12 months these features are fully developed. Fertility is first successful in females between 12-14 months-old

Indeed, in 1-year-old siblings, TL was significantly longer in males than females (males: 20.06 ± 0.6 cm, females: 17.78 ± 0.4 cm, n = 9), while SV remained constant (males: 9.8 ± 0.3 cm, females: 9.3 ± 0.3 cm, n = 9) (Fig 1C). In 2.5-month-old juvenile larvae siblings, TL did not differ (males: 4.7 ± 0.2 cm, females: 4.7 ± 0.2 cm, n = 12). This indicates that the differences in total length between sexes is due to an increased tail growth in males upon sexual maturation.

We then evaluated the post-embryonic development of the appendicular skeleton, particularly the long bones from the zeugopod. We used animals ranging from TL 4 to 20 cm, which represent axolotls from a juvenile stage to adulthood. Using alcian blue/alizarin red staining, we first evaluated the broad morphological changes in the skeleton. Alizarin red is a calcium-binding dye that is routinely used to detect ossification patterns together with alcian blue, which stains polysaccharides in cartilage. We observed a progressive expansion of the alizarin red staining in the skeletal elements, which starts in axolotls with a TL around 10-12 cm (Fig 1D). Still, the epiphyses of those elements remained cartilaginous in animals of TL 20 cm. Importantly, alizarin red also labels mineralized cartilage, which can be seen *in vivo* in axolotls by fluorescence imaging (Fig 1E), hence it does not provide accurate information on

160 the ossification dynamics. To accurately quantify ossified bone volume and trace the start of
161 the ossification process, we analyzed different limbs by µCT scan. Ossification was not
162 detected in animals of TL 10 cm. We observed the first appearance of an ossified ring around
163 both the radius and ulna in animals with a TL of 12 cm (Fig 1F). In animals bigger than 12 cm,
164 ossification extended longitudinally to both ends of the bone. Interestingly, the ossification
165 did not occur homogenously, but rather in a discontinuous manner. A porous appearance
166 resembles the mammalian bone development. In animals of TL ca 25 cm, this porosity
167 disappeared and the tissue became uniformly ossified (Fig 1H), forming compact bone.
168 Ossification extended to the epiphyses of the bone, as observed in the widening ends.
169 Quantification of the bone volumes (Fig 1G) are not significantly different between bones from
170 animals TL 12 and 14 cm, or TL 14 and 16 cm. However, between TL 16 cm and 20 cm, a 4-fold
171 increase in bone volume was observed for radius, and 7-fold for ulna. Moreover, radius
172 volume was significantly higher than ulna (1.4 times increase) in axolotls of TL 20 cm. Even
173 though ossification started when animals had a TL of 12 cm, there is variability between
174 siblings, specially at TL of 14 cm (Fig 1G). Whether this variability results from sexual
175 dimorphism or simply interindividual variation is yet to be determined.
176
177 **Axolotl bones are vascularized and the marrow cavity is filled with adipocytes**
178 Changes in the skeletal cellular landscape accompany the transition from a cartilage
179 anlage to bone. We assessed these changes in isolated radii from axolotls TL 6 and 12 cm,
180 which corresponded to radii before and during ossification. We performed H&E staining from
181 paraffin sections and observed that the radius was exclusively composed of chondrocytes in
182 animals TL 6 cm (Fig 2A, left panel). We identified a resting zone (RZ), filled with rounded
183 chondrocytes, a proliferative zone (PZ), characterized by flattened chondrocytes, and a
184 hypertrophic zone (HZ), where chondrocyte differentiation leads to an increase in cellular
185 volume. Interestingly, these zones were not uniformly organized, as opposed to the isotropic
186 cellular distribution of mammalian growth plates. The lack of an organized cellular distribution
187 has been previously observed in another salamander model (Quilhac et al., 2014). Throughout
188 the juvenile stages, a calcification ring surrounds the perichondral region of the HZ (arrowhead
189 Fig 2A', 3A). We have observed that the first calcification ring appears in development
190 occurred at stage 48 (data not shown). At this stage, the humerus is formed and the radius
191 and ulna had just started to form by bifurcation from the humerus distal end.

192 Radii from animals TL 12 cm (Fig 2A, right panel) have a similar cellular distribution of
193 the cartilage region as younger animals. But in contrast to young animals, we observed the
194 formation of a primary ossification center in the diaphysis, which contained a marrow cavity
195 surrounded by cortical bone. The woven-like bone seen on the µCT scan was also observed in
196 sections as discontinuous tissue surrounding the cartilage, with defined edges between gaps
197 (Fig 2A''). The bone extended beyond the marrow cavity, surrounding also the HZ. By TL 16
198 cm, radii stained with H&E showed a further progression in ossification. An expanding marrow
199 cavity and compact bone were also observed. However, cartilage lining subjacent to the bone
200 could still be seen suggesting that the transition to bone was not completed. Embedded
201 osteocytes in the cortical bone matrix and cells lining in the outer and inner sides of the bone
202 were observed (periosteum and endosteum respectively) (Fig 2B). In both TL 12 and 16 cm,
203 the marrow cavity was filled with adipocytes identified by their morphology.
204 A critical step for bone formation by endochondral ossification is the vascularization
205 of the tissue (Filipowska et al., 2017). To assess the vascularization of the skeletal elements
206 from animals TL 6 cm and 12 cm, we generated a new transgenic line that expresses EGFP
207 under the control of a *Tie2* promoter and enhancer (*Tie2-Tg*) (Schlaeger et al., 1997), labeling
208 blood vessels in the entire animal. We collected limbs from animals TL 6 cm and the radii from
209 animals TL 12 cm and performed whole-mount immunofluorescence (IF) against GFP,
210 followed by tissue clearing and confocal imaging. We observed that the blood vessels
211 surrounded the skeletal element of TL 6 cm animals, but the cartilage was not vascularized
212 (Fig 2C, left panel). However, we observed some blood vessel protrusions in close contact with
213 the perichondrium in the HZ (arrowhead, Fig 2D), which could point to the position where the
214 ossification of the skeletal element will start. In the radii of TL 12 cm animals (Fig 2C, right
215 panel), the mid-diaphysis was found to be vascularized, which correlates with the ossification
216 of the cartilage anlage and formation of the marrow cavity. We did not observe vascularization
217 of the epiphyses, and thus no secondary ossification center formation at this stage.
218
219 **Sox9 labels chondrogenic cells while Col1a2 labels all skeletal cells**
220 We have identified the morphological changes of the zeugopod skeleton during
221 growth. However, the identity of the cells within the skeletal tissue, and their origin, remains
222 unclear. A key transcription factor involved in cartilage development is Sox9 (Kozhemyakina
223 et al., 2015). Thus, using a *Sox9-Tg* knock in line, where a T2a self-cleaving peptide followed

224 by mCherry protein is fused to the endogenous SOX9 protein, we evaluated the distribution
225 of SOX9$^+$ cells in ulnas from animals TL 6 and 12 cm (Fig 3A). We confirmed that the expression
226 of mCherry mirrors the real expression of Sox9 by immunofluorescence (Fig 3C). In tissue
227 sections from TL 6 cm ulnas, most cells were mCherry$^+$, while perichondral cells were mCherry$^-$
228 (Fig 3A, left panel). We observed a similar distribution in ulnas from animals TL 12 cm (Fig 3A,
229 right panel), and we found no mCherry$^+$ cell in the ossified portion of the skeletal element (Fig
230 3D). Moreover, using a *Col1a2-Tg* line, we evaluated the distribution of COL1A2$^+$ cells in ulnas
231 from animals TL 6 and 12 cm (Fig 3B). This transgenic line expresses fluorescent protein TFP
232 under the control of the *Col1a2* enhancer and has been shown to label skeletal cells in the
233 axolotl (Gerber et al., 2018). We observed TFP$^+$ cells throughout the skeletal elements in both
234 sizes, labelling both cartilage and bone cells (Fig 3B, E), i.e. chondrocytes, perichondral cells,
235 osteoblasts, osteocytes and periosteal cells.
236
237 **Osteocalcin is expressed in bone cells and in some hypertrophic chondrocytes**
238 The most definite confirmation of ossification is the identification of mature
239 osteoblasts in the bone matrix and bone lining cells. To that end, we used immunodetection
240 of osteocalcin (anti-OCN). As expected, no labeling was observed in ulnas from TL 6 cm (Fig
241 4A, left panel), which further demonstrated the absence of bone tissue in juvenile larvae. In
242 TL 12 cm animals, we observed a broad OCN labeling of the bone ECM (Fig 4A, right panel).
243 We identified OCN$^+$ cells in the skeletal element both embedded in the bone matrix and in the
244 periosteum (arrowheads, Fig 4B). Interestingly, OCN$^+$ cells were also identified in the lower HZ
245 of the chondro-osseous junction of the mid-diaphysis. Those cells were mCherry$^+$, identified
246 by our *Sox9-Tg* line (solid arrowheads Fig 4B, 4C). Previous studies have correlated the
247 downregulation of *Sox9* in the HZ with the activation of the osteogenic program and the
248 persistence of SOX9 with an inhibition of bone-related markers (Dy et al., 2012; Lui et al.,
249 2019). The expression of OCN in HCs could point towards an early activation of an osteogenic
250 program in those cells. In that regard, osteocalcin expression has been reported in post-HCs
251 (Pullig et al., 2000). Some studies have demonstrated the ability of HCs to transdifferentiate
252 into osteoblasts in mammals and zebrafish (Giovannone et al., 2019; Yang et al., 2014).
253 However, the co-expression of SOX9 and OCN needs to be further explored.
254
255 **Lineage tracing reveals a contribution of *Col1a2*$^+$ cells to bone and adipocyte tissue**

256 Our above observations led us to hypothesize that some HCs could transdifferentiate
257 into bone cells in the axolotl. To test this idea, we evaluated the contribution of *Col1a2*$^{+}$
258 chondrocytes to bone formation.
259 Using the double transgenic *Col1a2xLPCherry-Tg*, we traced the fate of *Col1a2*$^{+}$ cells
260 by inducing the permanent labeling of chondrocytes by tamoxifen-induced conversion of the
261 Cre/Lox reporter cassette in TL 5 cm animals. In these animals the appendicular skeleton is
262 still exclusively cartilaginous. We allowed the animals to grow until a TL of 14 cm and we
263 collected the ulnas for sectioning and imaging. We observed a great proportion of the cells to
264 be mCherry^{+}. They were distributed through the cartilage part, bone matrix, periosteum,
265 endosteum and in the adipose tissue (Fig 4D, 4E). Moreover, we assessed whether some of
266 the mCherry^{+} cells were OCN^{+}. We found mCherry^{+}/OCN^{+} cells in the endosteum and
267 periosteum (arrowheads, Fig 4F, 4F', 4F''), showing that *Col1a2*$^{+}$ descendants gave rise, at
268 least partially, to committed osteoblast in the axolotl zeugopod. However, whether a specific
269 subpopulation of *Col1a2*$^{+}$ gives rise to all derived cells or if HCs contribute directly to OCN^{+}
270 cells, cannot be answered with this transgenic approach.
271
272 **Bone ossification and marrow cavity expand with age**
273 Axolotls have a life span extending to more than 20-years under controlled laboratory
274 conditions (Vieira et al., 2019). However, little is known about bone morphological features in
275 aged animals, although it is commonly assumed that axolotls retain cartilaginous epiphyses
276 and thus there is perennial longitudinal growth of the bones. We collected bones and limbs
277 from 1-, 5-, 7- year-old axolotls and our only available specimen of 20-years of age. In
278 histological sections from radii (Fig 5A), we observed an age-related expansion of the marrow
279 cavity towards the epiphyses. Cortical bone was also expanded longitudinally and radially,
280 surrounding most of the skeletal element length, even though some parts of the inner surface
281 of the epiphyses remained cartilaginous in most cases. However, when we sectioned the 20-
282 year-old radius (n = 1), we observed a partial ossification of the epiphysis (arrowhead, Fig 5A),
283 which suggests a continuous ossification of the radius with age. Importantly, we did not
284 identify a secondary ossification center in any of the radii analyzed. Still, we observed the
285 appearance of pseudo trabeculated bone tissue, which we believe corresponded to the
286 marrow cavity expansion. In addition, in whole limbs stained with alcian blue/alizarin red, we
287 observed a calcification in one of the carpal bones in a 5-year-old animal (Fig 5B), as well as

288 several tarsal bones in a 20-year-old animal (Fig 5C), which suggest that the short bones in the
289 autopod undergo a late ossification in comparison with the long bones in the zeugopod, but
290 also highlights the continuity of this process in adulthood and aging.

291 In elements from the stylopod and autopod (digits from 2-year old animals and humeri
292 from 5-year-old animals) (Fig 5D, E respectively), we observed the same features described
293 for long bones in the zeugopod, i.e., an ossified ring of cortical bone around a marrow cavity
294 filled with adipocyte tissue which expanded from the diaphysis towards the epiphyses.

295 This continuous ossification could be the origin of aberrant phenotypes. In 3 out of 6
296 bones from 7-year-old and in our single 20-year-old animal, we observed that the zeugopodial
297 bones were fused either in their proximal or distal epiphysis. In one case, the fusion occurred
298 with a heterotopic ossification and cartilage formation around the distal end of the radius.

299 Our results show a continuous ossification of the skeletal elements even in aged
300 animals. Whether the appendicular skeleton would become completely ossified if an animal
301 lived long enough remains unknown.

302

303 **Axolotl metamorphosis accelerates bone ossification**

304 Metamorphosis is a critical transformation in the life cycle of many amphibians. This
305 process allows them to access a vaster territory in their search for food and mating partners.
306 In some anurans and urodeles, ossification of the limb skeleton is associated with the
307 metamorphic transformation (Miura et al., 2008; Quilhac et al., 2014). Although axolotls are
308 neotenic and rarely undergo spontaneous metamorphosis, the administration of exogenous
309 thyroxine can induce it. We evaluated whether the ossification in axolotl is still responsive to
310 the hormonal changes of metamorphosis. If this is the case, metamorphosis should accelerate
311 the ossification process in axolotls. We injected thyroxine in axolotls TL 14 cm, where
312 ossification is already covering the mid-diaphysis. Radii were collected at 35 days post-
313 injection and embedded in paraffin for sectioning and staining. Metamorphic axolotls were
314 slightly smaller than their paedomorph siblings, although this difference was not significant
315 (paedomorph TL: 15.4 ± 0.4 cm, SV: 8.6 ± 0.3, n = 5, metamorphic TL: 14.7 ± 0.3, SV: 8.4 ± 0.5,
316 n = 6). By H&E staining, we did not observe differences in the gross morphology (Fig 6A)
317 compared to an un-injected animal. These observations are in agreement with a previous
318 study, in which no significant difference was observed in zeugopodial bones when surface and
319 length were compared between a pre- and post-metamorphic axolotl (Thampi et al., 2018).

However, when compared using µCT scan, we observed an increase in bone volume in metamorphic animals. Both zeugopodial bones had a bigger ossified area and the ossification pattern was more uniform than the paedomorph bones analyzed (Fig 6B). Bone volume quantification showed a significant increase of 4 times in radii volume and over 3 times increase for ulnas (Fig 6C). These results demonstrate that ossification is accelerated in axolotl limbs when metamorphosis is induced, and suggest that cells respond to intrinsic programs as well as hormonal changes.

352 **Discussion**

353

354 Appendicular skeletogenesis is considered highly conserved among tetrapods, mostly
355 based on studies in mammals and chicks, (Shubin et al., 1997) although the appendicular
356 skeleton has undergone species-specific adaptations due to the environmental influence.
357 Many species display variations in important cellular and temporal parameters of limb
358 development. Mammals are born with ossified bone, while most amphibians develop their
359 limbs post-embryonically. The transition of a cartilaginous appendicular skeleton to a bony
360 skeleton is associated with the hormonal changes during metamorphosis (Kemp and Hoyt,
361 1969; Rose and Reiss, 1993). Metamorphosis in amphibians is a significant event that precedes
362 sexual maturity, giving the animals a biological advantage. In neotenic salamanders, such as
363 the axolotl, the appendicular cartilage is not only a transitional tissue, and larvae live with a
364 calcified cartilage throughout their juvenile period. Their limbs ossify in the absence of
365 metamorphosis although it was proposed that the epiphyses remain cartilaginous throughout
366 life (Haines, 1942; Thampi et al., 2018) and that this feature would likely contribute to
367 longitudinal bone growth (Cosden-Decker et al., 2012). However, little can be said about the
368 biological clock triggering skeletal changes, since they rarely change to a terrestrial
369 environment.

370 In this work, we provide a characterization of the maturation of the appendicular
371 skeleton during the life span of the axolotl, considering ossification timing and age-related
372 effects, complementing previous studies in larval stages (Torok et al., 1998) and young adults
373 (Cosden-Decker et al., 2012). In our axolotl colony, animals are grown in fully standardized
374 conditions that allow us to use the total body length to associate it to appendicular changes
375 and biological landmarks such as sexual maturity. Our results show an exponential growth of
376 axolotls in the first 22-24 months of their life, after which growth plateaus. During this
377 exponential growth, animals become sexually mature and ossification of their appendicular
378 bones starts, but for most of the juvenile phase, axolotls present a mineralized ring around
379 the cartilaginous mid-diaphysis. Mineralization of the zeugopodial appendicular skeletal
380 elements was observed as early as developmental stage 48. In contrast, ossification starts
381 around the sexual maturity period, when we can observe the formation of a denser calcified
382 surface and embedded cells with morphological and genetic characteristics of osteoblasts.
383 Moreover, we show that *Col1a2*$^{+}$ cells or their progeny participate in the ossification process

384 by giving rise to osteogenic cells and adipocytes. We report a continuous ossification of
385 zeugopodial bones and marrow cavity expansion with age. However, this ossification is not
386 complete, as we observed a cartilage-bone composite in most of diaphyses analyzed. Short
387 bones, such as tarsals and carpals, undergo a very late ossification when compared to
388 appendicular long bones. Finally, we see an accelerated zeugopodial ossification in
389 metamorphic animals, indicating a responsiveness to exogenous thyroxine.
390
391 **Mineralization *versus* ossification**
392 For most of the initial larval stages, the skeleton is cartilaginous with mineral
393 deposition. We have observed calcification of the humeral diaphysis as early as Stage 48, when
394 radius and ulna had just started to form by bifurcation from the humerus distal end. Nye *et al*.
395 reported mineralization by alizarin red staining at stage 50, when condensations of the
396 metacarpals are already present (Nye et al., 2003). This discrepancy can be accounted for by
397 the detection protocol. While Nye *et al*., used processed samples, we used real-time vital
398 detection. The calcification of appendicular cartilage remains throughout the juvenile phase
399 of the axolotl until the anlage starts to ossify.
400 In contrast to mineralization, ossification occurs after the limbs are fully formed and
401 around the time animals begin to show secondary sexual characters. Generally, amphibian
402 metamorphosis precedes sexual maturation, while in neotenic amphibians both sexual
403 maturation and bone ossification occur in the absence of metamorphosis. In salamanders, as
404 in other species, metamorphosis provides adaptive features to change habitat and ensure
405 greater chances of survival. The axolotl and its geographically and phylogenetically related
406 counterpart, *Ambystoma velasci* (Parra-Olea et al., 2007; Shaffer and McKnight, 1996), are
407 examples of facultative metamorphs, which means that individuals transform into terrestrial
408 organisms when the environmental conditions of its habitat change. In *Xenopus laevis*
409 tadpoles lacking thyroid glands, metamorphosis is halted but growth continues and the
410 ossification progresses in the hind limb independently of thyroxine (Kerney et al., 2010). This
411 suggests that appendicular ossification programs could also be triggered in the absence of L-
412 thyroxine and that probably depends on a critical body mass. Although ossification genetic
413 programs in axolotl are triggered independently of metamorphosis, inducing metamorphosis
414 with exogenous thyroxine, accelerates the ossification process as shown in this work. Thus,
415 cells within the appendicular skeleton remain responsive to changes triggered by thyroxine.

416 In contrast to the fully ossified diaphysis of post-metamorphic limb newts (*Pleurodeles*
417 *waltl* total length 14 cm) (Quilhac et al., 2014), the diaphysis of axolotls retains a cartilage
418 anlage subjacent to the cortical bone even in old animals and also in post-metamorphic
419 zeugopodial and autopodial elements. We think this observation had eluded previous reports,
420 because most of them focus on the humerus or humeral-radial joint. We observed in humeri
421 of a 5-, 7- and 20-year-old animal only a modest cartilage layer in the diaphysis. Although in
422 *Xenopus*, the extent of ossification correlates with decreased regenerative potential, axolotls
423 can still regenerate their ossified limbs in paedomorph adults and induced land adults (Young
424 et al., 1985). However, both the potential for regeneration and its fidelity are reduced
425 (Monaghan et al., 2014).
426 Importantly, our results show that ossification in appendicular skeleton is continuous.
427 Rux *et al* observed some degree of ossification of the metaphysis in the femur of a 10-year-
428 old axolotl (Rux et al., 2018), which suggested that ossification of the appendicular bones
429 continues throughout life. Here, we have shown that this ossification reaches the epiphyses
430 with time.
431
432 **Contribution of COL1A2$^+$ cells during ossification**
433 One crucial difference between axolotl and mammalian bone formation is the
434 differential activation of the *Col1a2* enhancer. In mammals only osteoblasts activate the
435 *Col1a2* enhancer (Bou-Gharios et al., 1996), while in axolotls, chondrocytes show *Col1a2*
436 enhancer activity and *Col2a1* expression (Gerber et al., 2018; Khattak et al., 2013). We have
437 observed *Col1a2* enhancer activity as the first mesenchymal condensates form in the limb bud
438 (stage 47), and it remains active in cells inside the cartilage of long bones and in HCs at the
439 chondro-osseous junction even in 7-year-old animals (personal observation).
440 We consider that understanding the development of the appendicular bones is
441 essential to comprehend how limb regeneration is orchestrated in stages where different cell
442 types and different maturation stages are found at the amputation plane. The common use of
443 larval stage to study regeneration is normally preferred because it concludes faster and it is
444 easier to image.
445 One cell type largely ignored in regeneration is the adipocyte. We saw the contribution
446 of COL1A2$^+$ descendants to adipocytes in the marrow cavity. Although our *Col1a2-Tg* line also
447 labels periosteum, their contribution to homeostasis is typically restricted to skeletal cells.

448 Therefore, we speculate that the contribution of COL1A2$^+$ descendants to adipocytes is most
449 likely from chondrocytes. This result agrees with work done in zebrafish, in which lineage
450 tracing of chondrocytes has shown the contribution of these cells to the marrow adipocytes
451 (Giovannone et al., 2019), similar to what we show in this study. Lopez et al. have shown that
452 the axolotl bone marrow is nonhematopoietic in young adults (1-year-old) (Lopez et al., 2014).
453 Our study detects an adipocyte-filled marrow cavity in long bones of the zeugopod in young
454 and aged animals (Fig 2A, 2B, 5A).
455
456 **SOX9$^+$/OCN$^+$ cells**
457 During endochondral ossification, the fate of HCs was long considered to be death and
458 subsequent substitution for bone cells. Unexpectedly, we found that HCs at the chondro-
459 osseous junction are SOX9$^+$/OCN$^+$. OCN is a non-collagenous protein in the bone matrix
460 expressed and secreted by committed osteoblast. Although murine HCs can become
461 osteoblasts and osteocytes during endochondral bone formation (Giovannone et al., 2019;
462 Jing et al., 2017; Yang et al., 2014), it is surprising to find cells expressing both SOX9 and OCN.
463 SOX9 is known to block osteoblast differentiation and to maintain columnar chondrocyte
464 proliferation by delaying pre-hypertrophy, but also directing hypertrophic maturation (Dy et
465 al., 2012; Hattori et al., 2010; Lui et al., 2019). The roles of SOX9 are various, and its expression
466 in committed osteoblast has not been shown before, which suggests the presence of chondro-
467 osteogenic hybrid cells during the normal transition to the ossified skeleton in axolotl.
468 Chondro-osteogenic hybrids are found generally in reparative instances such as jaw
469 regeneration in zebrafish (Paul et al., 2016) and murine rib (Kuwahara et al., 2019) and may
470 hold an unexplored potential for bone regeneration. In future studies, with transgenic lines
471 labeling specifically HCs, we will be able to conclusively show their contribution to different
472 cell types in the axolotl skeleton.
473
474 **Perspectives**
475 The origin of adipocytes during ossification and their main role inside the marrow
476 cavity needs to be further explored in axolotls. The known role of bone marrow adipocytes is
477 to promote hematopoietic stem cell renewal. However, marrow cavity of axolotls remains
478 devoid of a hematopoietic niche (Lopez et al., 2014). We assume that the adipose tissue in the
479 marrow is white fat based on morphology and the fact that brown adipose tissue has not been

480 reported in amphibians (Gesta et al., 2007). As such, it is possible that these cells have instead,
481 an important role in osteogenesis and energy metabolism in the axolotl. Another cell type of
482 interest is the periskeletal cell. McCusker *et al*. had shown that the periskeletal tissue of older
483 animals of TL 25 cm is multilayered and more complex than that of larvae of TL 6.5 cm
484 (McCusker et al., 2016). Importantly, periskeletal tissue is mainly responsible for the
485 regeneration of the skeleton (Currie et al., 2016; McCusker et al., 2016). The high potential of
486 these cells has neither been tested in non-regenerative conditions, nor their origin and
487 contribution to the formation of appendicular bone has been investigated.
488
489 **Concluding remarks**
490 Taken together, our data provide evidence that bone remodeling is a continuous
491 process in axolotls, starting from a mineralized cartilaginous skeleton during the larval stage
492 to a slowly transitioning bone that continues to ossify as animals age. The bone ossification
493 occurs in the absence of thyroxine or a biomechanical challenge suggesting instead the
494 existence of a physiological timer either triggered by sexual maturation or body mass.
495 However, this ossification can be accelerated in response to exogenous thyroxine, creating in
496 short time a bone mass that would normally take longer to form. Our findings add to a growing
497 body of literature indicating that vertebrate skeletal tissues are structurally diverse, and break
498 many of the established mammalian-centric rules of development and maturation.
499
500
501
502
503
504
505
506
507
508
509
510
511

512 **Experimental procedures**

513

514 **Animal husbandry, transgenesis, metamorphosis and sample collection**

515 Axolotls (*Ambystoma mexicanum*) husbandry was performed in the CRTD axolotl
516 facility, following the guidelines previously published (Khattak et al. 2014). Husbandry and
517 experimental procedures were performed according to the Animal Ethics Committee of the
518 State of Saxony, Germany. Animals used were selected by its size and it is indicated in each
519 experiment individually (total length = TL; snout to vent = SV). Sex determination in juvenile
520 larvae was performed by PCR based on (Keinath et al., 2018).

521 White axolotls (*d/d*) were used for most of the experiments. Transgenic lines used
522 included the previously published TgSceI*(Mmus.Col1a2:TFPnls-T2a-ERT2-Cre-ERT2)*^{emt}
523 (referred as *Col1a2-Tg*) and TgSceI*(Mmus.Col1a2:TFPnls-T2a-ERT2-Cre-*
524 *ERT2;Mmus.CAGGS:lp-GFP-3pA-lp-Cherry)*^{emt} (referred as *Col1a2xLPCherry-Tg*) (Gerber et al.
525 2016). We generated the transgenic lines C-Ti$^{t/+}$*(Sox9:Sox9-T2a-mCherry)*^{emt} (referred as *Sox9-*
526 *Tg*) and TgTol2*(Mmus.Tie2:EGFP)*^{tsg} (referred as *Tie2-Tg*).

527 For generation of the *Tie2-Tg* transgenic line, we used the plasmid pSPTg.T2FXK (#54),
528 a gift from Thomas Sato (Addgene plasmid # 35963). The *Egfp* coding region was cloned 3´
529 from the promoter together with *Tol2* sequences. Fertilized embryos from *d/d* axolotls were
530 injected with the *Tie2:EGFP* vector and *Tol2* mRNA as previously described (Khattak et al.
531 2014). The *Sox9-Tg* reporter line is a targeted Knock-in line created by CRISPR/Cas9 technology
532 according to the published protocol (Fei et al., 2018). Briefly, a portion of the Sox9 gene
533 including a part of the second (last) intron and the remaining downstream part of the CDS was
534 PCRed from the axolotl genomic DNA and inserted into the vector pGEM-T along with a DNA
535 fragment encoding T2a-Cherry-3xnls. The resulting vector was injected into fertilized eggs
536 along with the CAS9 protein and the gRNA targeting the sequence
537 GGACTGCTGGCGAATGCACC, which is found in the intron sequence within the vector and in
538 the genome. As a result, mCherry fused to the C-terminus of the SOX9 and separated by a T2a
539 self-cleaving peptide is expressed from the endogenous SOX9 genomic locus.

540 Metamorphosis was induced in *d/d* animals as previously described (Khattak et al.,
541 2014). Briefly, axolotls TL 14 cm were anesthetized prior to intraperitoneal injections with 1.5
542 µL of L-thyroxine (Sigma, T2376) per gram of bodyweight (stock 1 µg/µL in DMSO). Animals

543 were cleaned regularly and water level was reduced as gills were lost. Only 1 out of 15 animals
544 died during metamorphosis. Tissue was collected at 35 days post injection.
545 Recombination of *Col1a2xLPCherry-Tg* was induced by keeping animals in separated
546 tanks with water containing (Z)-4-hydroxytamoxifen (4-OHT, Sigma T5648) 2 µM overnight.
547 Animals were then washed and screened two weeks later to ensure conversion.
548 For tissue collection, animals were anesthetized with 0.007% benzocaine solution.
549 After collection, animals were euthanized by exposing them to. a lethal dosage of anesthesia
550 (0.1% benzocaine) for at least 20 min.
551
552 **Alcian blue/alizarin red staining**
553 Limbs collected were fixed with formaldehyde 10% at 4°C for 1 week and then washed
554 three times with PBS 1x and dehydrated with serial EtOH washes (25, 50 and 70%). Limbs were
555 either stored at -20°C in EtOH 70% or processed immediately at RT. Epidermis from animals >
556 12 cm TL was removed. Limbs were stained with alcian blue solution (Sigma A3157; alcian blue
557 0.0001% in EtOH 60% / glacial acetic acid 40%) for 3 days. Then, samples were rehydrated
558 with EtOH dilution series in H_2O (80, 70, 50, 25%), before treatment with trypsin 1% in borax
559 30% for 30 min. Limbs were rinsed with KOH 1% and stained with alizarin red solution (Sigma
560 A5533; alizarin red 0.0001% in KOH 1%) for 3 days. Next, limbs were washed with KOH 1% and
561 cleared in KOH 1% / glycerol 20% overnight. Finally, limbs were dehydrated with EtOH dilution
562 series (25, 50, 70, 90 and 3x 100%) and later transferred into serial washes of glycerol/EtOH
563 (1:3, 1:1 and 3:1). Limbs were stored in 100% glycerol at 4°C.
564
565 **µCT scan**
566 Limbs collected were fixed with formaldehyde 10% at 4°C for 1 week and then washed
567 three times with PBS 1x and dehydrated with serial EtOH washes (25, 50 and 70%) and stored
568 in EtOH 70% at -20°C until measurement. Bone volume and microarchitecture were
569 determined by micro-computed tomography (µCT, vivaCT40, ScancoMedical) of zeugopodial
570 bones using pre-defined script 6. The isotropic voxel size was 10.5 µm (70 kVp, 114 µA, 200
571 ms integration time). Diaphysis scans were done for the whole zeugopod (both elements at
572 the same time) and included 600 – 1000 slices. ScancoMedical protocols were used for all
573 analyses and 3D reconstructions. Threshold used for analyses in Fig. 1 was 220 mg HA/cm^3,
574 and for Fig. 6 was 150 mg HA/cm^3.

575

576 **Paraffin sectioning and H&E staining**

577 Skeletal elements were isolated and fixed with MEMFa 1x (MOPS 0.1M pH7.4 / EGTA
578 2mM / MgSO4x7H2O 1mM / 3.7% formaldehyde) overnight at 4°C, washed with PBS 1x and
579 decalcified with EDTA 0.5M pH7.4 at 4°C for 1 to 4 weeks. After decalcification, samples were
580 washed with PBS 1x and dehydrated with serial EtOH washes (25, 50, 70 and x3 100%).
581 Samples were then incubated 3x with Roti®Histol (Carl Roth, 6640) at RT and 4x with paraffin
582 at 65°C in glass containers. After last incubation, samples were embedded in paraffin (Roti®-
583 Plast, Carl Roth, 6642) using plastic containers and stored at RT. Longitudinal sections of 6 µM
584 thickness were obtained.

585 H&E staining on paraffin sections was performed following the producer
586 recommendations (Sigma, Procedure No. HHS)

587

588 **Cryosectioning and immunofluorescence**

589 Skeletal elements were isolated and fixed with MEMFa 1x overnight at 4°C, washed
590 with PBS 1x and decalcified with EDTA at 4°C for 48 hours. Next, the skeletal elements were
591 washed with PBS 1x and dehydrated overnight with sucrose 30% at 4°C. Samples were
592 embedded in O.C.T. compound (Tissue-Tek, 4583) using plastic molds and frozen with dry ice
593 for 1 hour prior to storage at -20°C. Longitudinal sections of 12 µm thickness were cut and
594 mounted on superfrost slides. Slides were kept at -20°C until processed.

595 For immunofluorescence, slides were dried at RT for at least 1 hour. Sections were
596 washed 3x with PBS 1x + 0.3% Tx-100 prior to blocking with PBS 1x + 0.3% Tx-100 + 10% normal
597 horse serum for 1 hour. Primary antibody incubation was done in blocking solution overnight
598 at 4°C. Sections were then washed 3x with PBS 1x + 0.3% Tx-100 and incubated with secondary
599 antibody 1:300 and nuclear staining 1:10.000 for 2 hours. Finally, sections were washed 3x
600 with PBS 1x + 0.3% Tx-100 and mounted using Mowiol mounting medium (Carl Roth, 0713).
601 The antibodies and nuclear stainings used in this work are listed in table I.

602

603 **Whole mount immunofluorescence and tissue clearing**

604 Limbs or isolated skeletal elements were fixed with MEMFa 1x overnight at 4°C,
605 washed with PBS 1x and decalcified with EDTA at 4°C for 48 hours. Whole mount
606 immunofluorescence protocol was adapted from (Masselink et al., 2019). Briefly, skeletal

607 elements were washed overnight with PBS 1x + 0.3% Tx-100 at RT and then blocked in PBS +
608 0.3% Tx-100 + 10% DMSO + 5% goat serum for 24 hours at 37°C. Samples were incubated with
609 primary antibody anti-GFP in blocking solution for 3 days at 37°C. Next, samples were briefly
610 rinsed with PBS + 0.3% Tx-100 and then washed 4x for 2 hours at 37°C. Samples were blocked
611 again at 37°C overnight and then incubated with secondary antibody for 2 days at 37°C. After
612 incubation, samples were rinsed with PBS + 0.3% Tx-100 and then washed 2x for 2 hours at
613 37°C. Nuclear staining was done for 1 hour in washing solution at RT and samples were then
614 washed 4x in PBS 1x for 15 min at RT. Isolated skeletal elements were embedded in agarose
615 1% before clearing.

616 For clearing, samples were dehydrated with serial washes of EtOH (25, 50, 70, 100%)
617 for 2 hours each at 4°C. Samples were then incubated overnight in EtOH 100% at 4°C prior to
618 clearing with ethyl cinnamate (Sigma, 112372-100G) at RT for at least 2 hours. Samples were
619 imaged the same day. The antibodies and nuclear stainings used in this work are listed in table
620 I.

621

622 Table I: Antibodies and nuclear staining.

Antibody / Nuclear Staining	Dilution	Cat. Number
Anti-GFP (chicken)	1:500	Abcam (ab13970)
Anti-OCN (rabbit)	1:250	Abcam (ab198228)
Goat anti-Rabbit, Alexa Fluor 647	1:300	Invitrogen (A-21245)
Goat anti-Chicken, Alexa Fluor 488	1:1000	Invitrogen (A-11039)
TO-PRO™-3 iodide (642/661)	1:10.000	Invitrogen (T3605)
SYTOX™ Green nucleic acid stain	1:10.000	Invitrogen (S7020)

623

624 **Microscopy**

625 Alcian blue/alizarin red staining imaging was performed on a Zeiss Discovery.V20
626 stereomicroscope (Plan S 1.0x). H&E staining imaging was performed on a Zeiss Axio
627 Observer.Z1 inverted microscope (Plan-apochromat 20x/0.8). Immunofluorescence imaging
628 was performed on a Zeiss Axio Observer.Z1 inverted microscope with an ApoTome1 system
629 (Plan-apochromat 10x/0.45) and on a Zeiss confocal laser scanning microscope LSM 780 (Plan-
630 apochromat 10x/0.45 or Plan-apochromat 20x/0.8). Whole mount immunofluorescence

imaging was performed on a Zeiss confocal laser scanning microscope LSM780 (Plan apochromat 10x/0.45).

Statistical analysis

Statistical analysis was performed using the software Prism9 (GraphPad Software, LLC) for macOS. To assess the differences in TL or SV between sexes (Fig 1C), a paired t test was performed between samples. To assess the differences in volume between radii and ulnas of different TL animals (Fig 1G) and between radii and ulnas of paedomorph and metamorphic animals (Fig 6C), a Two-way ANOVA test was performed, using a post hoc Tukey's multiple comparisons test for assessing statistical significance between each sample pair. P-values < 0.05 were considered statistically significant.

Acknowledgements

We would like to thank Elly M. Tanaka for providing the *Sox9-Tg* line and Joshua D. Currie for guidance during the creation of the *Tie2-Tg* line. We thank Prof. Lorenz Hofbauer, Osvaldo Contreras and Rita Aires for proof-reading this paper and valuable comments. We thank all members of the Sandoval-Guzmán Lab for continuous support during the development of this work. We also would like to thank Anja Wagner and Beate Gruhl for their valuable dedication to the axolotl care. Camilo Riquelme-Guzmán was supported by the DIGS-BB Fellow award and DFG Research Grant (SA 3349/3-1). This work was supported by the Light Microscopy Facility, a Core Facility of the CMCB Technology Platform at TU Dresden.

Authors contribution

CRG and TSG conceived experiments, analysed data and wrote the manuscript. CRG conducted experiments. MR, MS and AB contributed experimental data and support. DK created *Sox9-Tg* line. DK and MR contributed with manuscript revision and discussions. TSG secured funding for the project.

663 **References**

664

665 Bou-Gharios, G., Garrett, L.A., Rossert, J., Niederreither, K., Eberspaecher, H., Smith, C.,
666 Black, C., and Crombrugghe, B. (1996). A potent far-upstream enhancer in the mouse pro
667 alpha 2(I) collagen gene regulates expression of reporter genes in transgenic mice. J Cell
668 Biology *134*, 1333–1344.

669 Cosden-Decker, R.S., Bickett, M.M., Lattermann, C., and MacLeod, J.N. (2012). Structural and
670 functional analysis of intra-articular interzone tissue in axolotl salamanders. Osteoarthritis
671 and Cartilage *20*, 1347–1356.

672 Currie, J.D., Kawaguchi, A., Traspas, R., Schuez, M., Chara, O., and Tanaka, E.M. (2016). Live
673 Imaging of Axolotl Digit Regeneration Reveals Spatiotemporal Choreography of Diverse
674 Connective Tissue Progenitor Pools. Developmental Cell *39*, 411–423.

675 Dy, P., Wang, W., Bhattaram, P., Wang, Q., Wang, L., Ballock, R.T., and Lefebvre, V. (2012).
676 Sox9 Directs Hypertrophic Maturation and Blocks Osteoblast Differentiation of Growth Plate
677 Chondrocytes. Dev Cell *22*, 597–609.

678 Fei, J.-F., Lou, W.P.-K., Knapp, D., Murawala, P., Gerber, T., Taniguchi, Y., Nowoshilow, S.,
679 Khattak, S., and Tanaka, E.M. (2018). Application and optimization of CRISPR–Cas9-mediated
680 genome engineering in axolotl (Ambystoma mexicanum). Nat Protoc *13*, 2908–2943.

681 Filipowska, J., Tomaszewski, K.A., Niedźwiedzki, Ł., Walocha, J.A., and Niedźwiedzki, T.
682 (2017). The role of vasculature in bone development, regeneration and proper systemic
683 functioning. Angiogenesis *20*, 291–302.

684 Gerber, T., Murawala, P., Knapp, D., Masselink, W., Schuez, M., Hermann, S., Gac-Santel, M.,
685 Nowoshilow, S., Kageyama, J., Khattak, S., et al. (2018). Single-cell analysis uncovers
686 convergence of cell identities during axolotl limb regeneration. Science eaaq0681.

687 Gesta, S., Tseng, Y.-H., and Kahn, C.R. (2007). Developmental Origin of Fat: Tracking Obesity
688 to Its Source. Cell *131*, 242–256.

689 Giovannone, D., Paul, S., Schindler, S., Arata, C., Farmer, D.T., Patel, P., Smeeton, J., and
690 Crump, G.J. (2019). Programmed conversion of hypertrophic chondrocytes into osteoblasts
691 and marrow adipocytes within zebrafish bones. ELife *8*.

692 Haines, R.W. (1942). The Evolution of Epiphyses and of Endochondral Bone. Biol Rev Camb
693 Philos Soc.

694 Hattori, T., Müller, C., Gebhard, S., Bauer, E., Pausch, F., Schlund, B., Bösl, M.R., Hess, A.,
695 Surmann-Schmitt, C., Mark, H. von der, et al. (2010). SOX9 is a major negative regulator of
696 cartilage vascularization, bone marrow formation and endochondral ossification.
697 Development *137*, 901–911.

698 Jing, Y., Jing, J., Ye, L., Liu, X., Harris, S.E., Hinton, R.J., and Feng, J.Q. (2017). Chondrogenesis
699 and osteogenesis are one continuous developmental and lineage defined biological process.
700 Scientific Reports *7*, 10020.

701 Keinath, M.C., Timoshevskaya, N., Timoshevskiy, V.A., Voss, S.R., and Smith, J.J. (2018).
702 Miniscule differences between sex chromosomes in the giant genome of a salamander. Sci
703 Rep-Uk *8*, 17882.

704 Kemp, N.E., and Hoyt, J.A. (1969). Sequence of ossification in the skeleton of growing and
705 metamorphosing tadpoles of Rana pipiens. J Morphol *129*, 415–443.

706 Kerney, R., Wassersug, R., and Hall, B.K. (2010). Skeletal advance and arrest in giant non-
707 metamorphosing African clawed frog tadpoles (Xenopus laevis: Daudin). J Anat *216*, 132–
708 143.

709 Khattak, S., Schuez, M., Richter, T., Knapp, D., Haigo, S.L., Sandoval-Guzmán, T., Hradlikova,
710 K., Duemmler, A., Kerney, R., and Tanaka, E.M. (2013). Germline transgenic methods for
711 tracking cells and testing gene function during regeneration in the axolotl. Stem Cell Reports
712 *1*, 90–103.

713 Khattak, S., Murawala, P., Andreas, H., Kappert, V., Schuez, M., Sandoval-Guzmán, T.,
714 Crawford, K., and Tanaka, E.M. (2014). Optimized axolotl (Ambystoma mexicanum)
715 husbandry, breeding, metamorphosis, transgenesis and tamoxifen-mediated recombination.
716 Nat Protoc *9*, 529–540.

717 Kozhemyakina, E., Lassar, A.B., and Zelzer, E. (2015). A pathway to bone: signaling molecules
718 and transcription factors involved in chondrocyte development and maturation.
719 Development (Cambridge, England) *142*, 817–831.

720 Kragl, M., Knapp, D., Nacu, E., Khattak, S., Maden, M., Epperlein, H., and Tanaka, E.M.
721 (2009). Cells keep a memory of their tissue origin during axolotl limb regeneration. Nature
722 *460*, 60–65.

723 Kuwahara, S.T., Serowoky, M.A., Vakhshori, V., Tripuraneni, N., Hegde, N.V., Lieberman, J.R.,
724 Crump, J.G., and Mariani, F.V. (2019). Sox9+ messenger cells orchestrate large-scale skeletal
725 regeneration in the mammalian rib. Elife *8*, e40715.

726 Lopez, D., Lin, L., Monaghan, J.R., Cogle, C.R., Bova, F.J., Maden, M., and Scott, E.W. (2014).
727 Mapping hematopoiesis in a fully regenerative vertebrate: the axolotl. Blood *124*, 1232–
728 1241.

729 Lui, J.C., Yue, S., Lee, A., Kikani, B., Temnycky, A., Barnes, K.M., and Baron, J. (2019).
730 Persistent Sox9 expression in hypertrophic chondrocytes suppresses transdifferentiation into
731 osteoblasts. Bone *125*, 169–177.

732 Malacinski, G.M. (1978). The Mexican Axolotl, Ambystoma mexicanum: Its Biology and
733 Developmental Genetics, and Its Autonomous Cell-lethal Genes. Integr Comp Biol *18*, 195–
734 206.

735 Masselink, W., Reumann, D., Murawala, P., Pasierbek, P., Taniguchi, Y., Bonnay, F., Meixner,
736 K., Knoblich, J.A., and Tanaka, E.M. (2019). Broad applicability of a streamlined Ethyl
737 Cinnamate-based clearing procedure. Development *146*, dev.166884.

738 McCusker, C.D., Diaz-Castillo, C., Sosnik, J., Phan, A.Q., and Gardiner, D.M. (2016). Cartilage
739 and bone cells do not participate in skeletal regeneration in Ambystoma mexicanum limbs.
740 Developmental Biology *416*, 26–33.

741 Miura, S., Hanaoka, K., and Togashi, S. (2008). Skeletogenesis in Xenopus tropicalis:
742 Characteristic bone development in an anuran amphibian. Bone *43*, 901–909.

743 Monaghan, J.R., Stier, A.C., Michonneau, F., Smith, M.D., Pasch, B., Maden, M., and Seifert,
744 A.W. (2014). Experimentally induced metamorphosis in axolotls reduces regenerative rate
745 and fidelity. Regen *1*, 2–14.

746 Nye, H.L.D., Cameron, J.A., Chernoff, E.A.G., and Stocum, D.L. (2003). Extending the table of
747 stages of normal development of the axolotl: Limb development. Dev Dynam *226*, 555–560.

748 Olsen, B., Reginato, A., and Wang, W. (2000). Bone development. Annual Review of Cell and
749 Developmental Biology *16*, 191–220.

750 Parra-Olea, G., Recuero, E., and Zamudio, K.R. (2007). Polymorphic microsatellite markers for
751 Mexican salamanders of the genus Ambystoma. Mol Ecol Notes *7*, 818–820.

752 Paul, S., Schindler, S., Giovannone, D., Terrazzani, A. de M., Mariani, F.V., and Crump, J.G.
753 (2016). Ihha induces hybrid cartilage-bone cells during zebrafish jawbone regeneration.
754 Development *143*, 2066–2076.

755 Pullig, O., Weseloh, G., Ronneberger, D.-L., Käkönen, S.-M., and Swoboda, B. (2000).
756 Chondrocyte Differentiation in Human Osteoarthritis: Expression of Osteocalcin in Normal
757 and Osteoarthritic Cartilage and Bone. Calcified Tissue Int *67*, 230–240.

758 Quilhac, A., Ricqlès, A., Lamrous, H., and Zylberberg, L. (2014). Globuli ossei in the long limb
759 bones of Pleurodeles waltl (Amphibia, Urodela, Salamandridae). J Morphol *275*, 1226–1237.

760 Rose, C.S., and Reiss, J.O. (1993). Metamorphosis and the vertebrate skull: ontogenetic
761 patterns and developmental mechanisms. In The Skull, J. Hanken, and B.K. Hall, eds.
762 (University of Chicago Press), pp. 289–346.

763 Rozenblut, B., and Ogielska, M. (2005). Development and growth of long bones in European
764 water frogs (Amphibia: Anura: Ranidae), with remarks on age determination. J Morphol *265*,
765 304–317.

766 Rux, D., Decker, R.S., Koyama, E., and Pacifici, M. (2018). Joints in the appendicular skeleton:
767 Developmental mechanisms and evolutionary influences. Curr Top Dev Biol *133*, 119–151.

768 Schlaeger, T.M., Bartunkova, S., Lawitts, J.A., Teichmann, G., Risau, W., Deutsch, U., and
769 Sato, T.N. (1997). Uniform vascular-endothelial-cell-specific gene expression in both
770 embryonic and adult transgenic mice. Proc National Acad Sci *94*, 3058–3063.

Schreckenberg, G.M., and Jacobson, A.G. (1975). Normal stages of development of the axolotl, Ambystoma mexicanum. Dev Biol *42*, 391–399.

Shaffer, H.B., and McKnight, M.L. (1996). The Polytypic Species Revisited: Genetic Differentiation and Molecular Phylogenetics of the Tiger Salamander Ambystoma tigrinum (Amphibia: Caudata) Complex. Evolution *50*, 417.

Shubin, N., Tabin, C., and Carroll, S. (1997). Fossils, genes and the evolution of animal limbs. Nature *388*, 639–648.

Thampi, P., Liu, J., Zeng, Z., and MacLeod, J.N. (2018). Changes in the appendicular skeleton during metamorphosis in the axolotl salamander (Ambystoma mexicanum). Journal of Anatomy *233*, 468–477.

Torok, M.A., Gardiner, D.M., Shubin, N.H., and Bryant, S.V. (1998). Expression of HoxD Genes in Developing and Regenerating Axolotl Limbs. Dev Biol *200*, 225–233.

Vieira, W.A., Wells, K.M., and McCusker, C.D. (2019). Advancements to the Axolotl Model for Regeneration and Aging. Gerontology 1–11.

Wolfe, A., Nye, H., and Cameron, J. (2000). Extent of ossification at the amputation plane is correlated with the decline of blastema formation and regeneration in Xenopus laevis hindlimbs. Developmental Dynamics : An Official Publication of the American Association of Anatomists *218*, 681–697.

Yang, L., Tsang, K., Tang, H., Chan, D., and Cheah, K.S. (2014). Hypertrophic chondrocytes can become osteoblasts and osteocytes in endochondral bone formation. Proceedings of the National Academy of Sciences *111*, 12097–12102.

Young, H.E., Bailey, C.F., Markwald, R.R., and Dalley, B.K. (1985). Histological analysis of limb regeneration in postmetamorphic adult Ambystoma. Anatomical Rec *212*, 183–194.

801 **Figure legends**

802

803 **Figure 1: Appendicular skeleton is ossified with growth**

804

805 (A) Quantification of axolotl total length (TL) in cm as a function of its age in months. Animal
806 sex was not considered (n = 213). Y-axis scale was set to logarithmic scale to better represent
807 the growth phases.
808 (B) Quantification of axolotl snout to vent length (SV) in cm as a function of its age in months.
809 Animal sex was not considered (n = 213). Y-axis scale was set to logarithmic scale to better
810 represent the growth phases.
811 (C) Quantification of TL and SV in cm in 1-year-old siblings as a function of its sex. (n = 18. 9
812 males, 9 females. *** $p < 0.001$, student's t test).
813 (D) Alcian blue/alizarin red staining of limbs from different TL animals. R: radius, U: ulna. Scale
814 bar for 4 and 10 cm: 500 µm. Scale bar for 12 to 20 cm: 1 mm.
815 (E) *In vivo* alizarin red staining of axolotl TL 5 cm. Scale bar: 500 µm
816 (F) 3D reconstructions from µCT scan for zeugopodial bones from different TL animals. All
817 bones are scaled. Scale bar: 250 µm.
818 (G) Quantification of zeugopodial bones volume (cm^3) from different TL animals. (n = 4 per
819 size. a: radius TL 20 cm compared to radius from TL 10, 12, 14 and 16 cm. b: ulna TL 20 cm
820 compared to ulna from TL 10, 12, 14 and 16 cm. c: radius TL 20 cm compared to ulna TL 20
821 cm. a, b: $p < 0.001$, c: $p < 0.05$, Tukey's multiple comparisons test).
822 (H) 3D reconstruction from µCT scan for zeugopodial bones from axolotl TL 25 cm. Bones
823 scaled to (E). Scale bar: 500 µm.

824

825

826

827

828

829

830

831

832

833 **Figure 2: Bone is vascularized and marrow cavity is filled with adipocytes**

834

835 (A) Representative sections of radii stained with H&E from axolotls TL 6 and 12 cm. RZ: resting
836 zone, PZ: proliferative zone, HZ: hypertrophic zone, MC: marrow cavity, D: distal, P: proximal.
837 Scale bar: 500 µm.
838 (A') Inset from TL 6 cm in (A). Arrowhead: calcified ring around HZ. Scale bar: 250 µm
839 (A'') Inset from TL 12 cm in (A). Arrowhead: discontinuous ossification around diaphysis. Scale
840 bar: 250 µm
841 (B) H&E staining in the distal half of the radius from an axolotl TL 16 cm. Scale bar: 500 µm.
842 (C) Confocal image of anti-GFP whole-mount IF from forelimb or radius from *Tie2-Tg* (red) TL
843 6 or 12 cm respectively. TO-PRO™3 was used for nuclear staining (white). Image represents a
844 maximum intensity projection of 3 images (10 µm interval). Arrowheads: bone vascularization.
845 Scale bar: 250 µm.
846 (D) Inset from *Tie2-Tg* TL 6 cm in (C) with overlapping brightfield image. Arrowhead: blood
847 vessel in contact with calcified cartilage. Scale bar: 100 µm.

848

849

850

851

852

853

854

855

856

857

858

859

860

861

862

863

864

865 **Figure 3: Sox9 labels chondrogenic cells while Col1a2 labels all skeletal cells**

866

867 (A) Confocal image of ulnas sections from *Sox9-Tg* (red) axolotls TL 6 and 12 cm. Calcified
868 tissue stained with calcein (green). TO-PRO™3 was used for nuclear staining (white). D: distal,
869 P: proximal. Scale bar: 250 µm.
870 (B) Confocal image of ulna sections from *Col1a2-Tg* (red) axolotls TL 6 and 12 cm. TO-PRO™3
871 was used for nuclear staining (white). Scale bar: 250 µm.
872 (C) Confocal image of anti-Sox9 IF in ulna sections from *Sox9-Tg* in axolotl TL 16 cm. SYTOX™
873 Green was used for nuclear staining. Scale bar: 250 µm
874 (D) Inset from (A), *Sox9-Tg* TL 12 cm. Dotted line shows boundary between cartilage and bone
875 (chondro-osseous junction), hc: hypertrophic chondrocytes. Scale bar: 250 µm.
876 (E) Inset from (B) *Col1a2-Tg* TL 12 cm, os: osteocyte, eo: endosteal cell, hc: hypertrophic
877 chondrocytes. Scale bar: 250 µm.

878
879
880
881
882
883
884
885
886
887
888
889
890
891
892
893
894
895
896

897 **Figure 4: Col1a2^{+} cells contribute to OCN^{+} osteoblasts**

898

899 (A) Confocal image of anti-OCN IF (red) from representative radii sections from axolotls TL 6
900 and 12 cm. SYTOX™ Green was used for nuclear staining (white). D: distal, P: proximal. Scale
901 bar: 250 µm.
902 (B) Inset from (A) anti-OCN IF (red). Dotted line shows boundary between cartilage and bone.
903 Solid arrowheads: hypertrophic chondrocytes. Arrowheads: periosteal cells.
904 (C) Confocal image of anti-OCN IF from radii sections from *Sox9-Tg* TL 12 cm animals. SYTOX™
905 Green was used for nuclear staining . Scale bar: 250 µm.
906 (D) Confocal image of *Col1a2xLPCherry-Tg* (red) ulna sections from tamoxifen-converted
907 axolotls at TL 5 cm and grown to TL 14 cm. SYTOX™ Green was used for nuclear staining
908 (white). Dotted line shows boundary between cartilage and bone, c: cartilage, b: bone, mc:
909 marrow cavity. Scale bar: 250 µm.
910 (E) Confocal image of *Col1a2xLPCherry-Tg* (red) ulna sections from axolotls TL 14 cm. SYTOX™
911 Green was used for nuclear staining (white), po: periosteum, eo: endosteum, ad: adipocytes.
912 Scale bar: 100 µm.
913 (F, F', F'') Confocal image of anti-OCN IF (green) (F) from ulna sections from *Col1a2xLPCherry-*
914 *Tg* (red) (F') axolotls TL 14 cm. SYTOX™ Green was used for nuclear staining (white). (F'')
915 Merge. Scale bar: 100 µm.

916
917
918
919
920
921
922
923
924
925
926
927
928

929 **Figure 5: Bone ossification and marrow cavity expand with age**

930

931 (A) H&E staining of radii sections from different age axolotls. D: distal, P: proximal, ep:
932 epiphysis, mc: marrow cavity, b: bone. Scale bar: 500 µm.
933 (B) Alcian blue/alizarin red staining of forelimb from a 5-year-old axolotl. Scale bar: 2 mm.
934 (C) Alcian blue/alizarin red staining of foot from a 20-year-old axolotl. Scale bar: 2 mm.
935 (D) H&E staining of proximal phalanx from 2-year-old axolotl. Scale bar: 1 mm.
936 (E) H&E staining of humerus from 5-year-old axolotl. Scale bar: 1 mm.

937
938
939
940
941
942
943
944
945
946
947
948
949
950
951
952
953
954
955
956
957
958
959
960

961 **Figure 6: Axolotl metamorphosis accelerates bone ossification**

962

963 (A) H&E staining from radii sections from paedomorphic and metamorphic axolotls (35 dpi).
964 D: distal, P: proximal. Scale bar: 500 µm.
965 (B) 3D reconstructions from µCT scans for zeugopodial bones from aquatic and metamorphic
966 axolotl. All bones are scaled. Scale bar: 500 µm.
967 (C) Quantification of zeugopodial bones volume (cm^3) from aquatic and metamorphic axolotl.
968 (n = 5 for aquatic zeugopods and n = 6 for metamorphic zeugopods. ** $p < 0.01$, * $p < 0.05$,
969 student's t test).

970

971

972

973

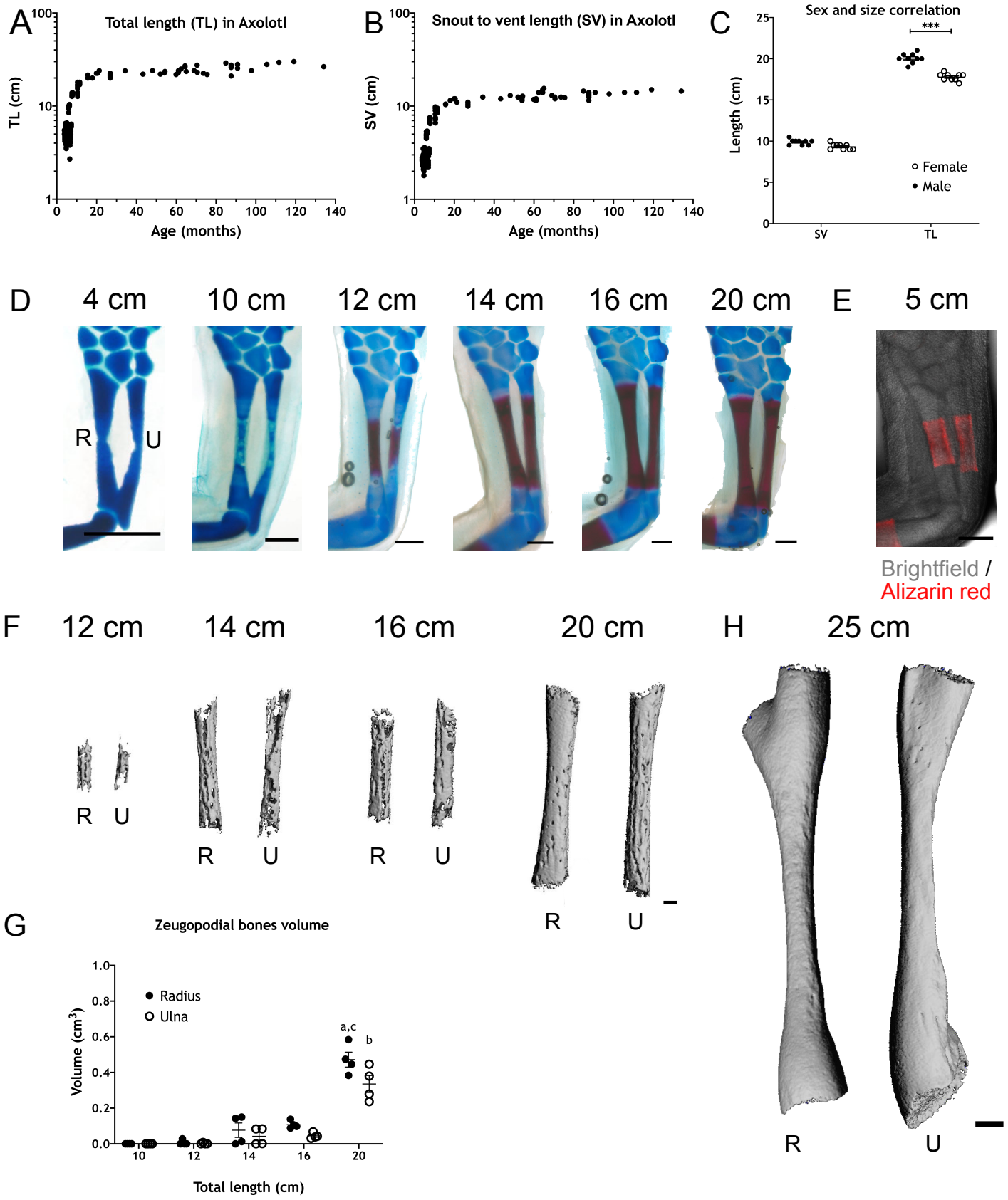
A
Total length (TL) in Axolotl
TL (cm)
Age (months)
B
Snout to vent length (SV) in Axolotl
SV (cm)
Age (months)
C
Sex and size correlation
***
Length (cm)
Female
Male
SV
TL
D
4 cm
10 cm
12 cm
14 cm
16 cm
20 cm
R
U
E
5 cm
Brightfield /
Alizarin red
F
12 cm
14 cm
16 cm
20 cm
R
U
H
25 cm
G
Zeugopodial bones volume
Radius
Ulna
Volume (cm³)
a,c
b
Total length (cm)

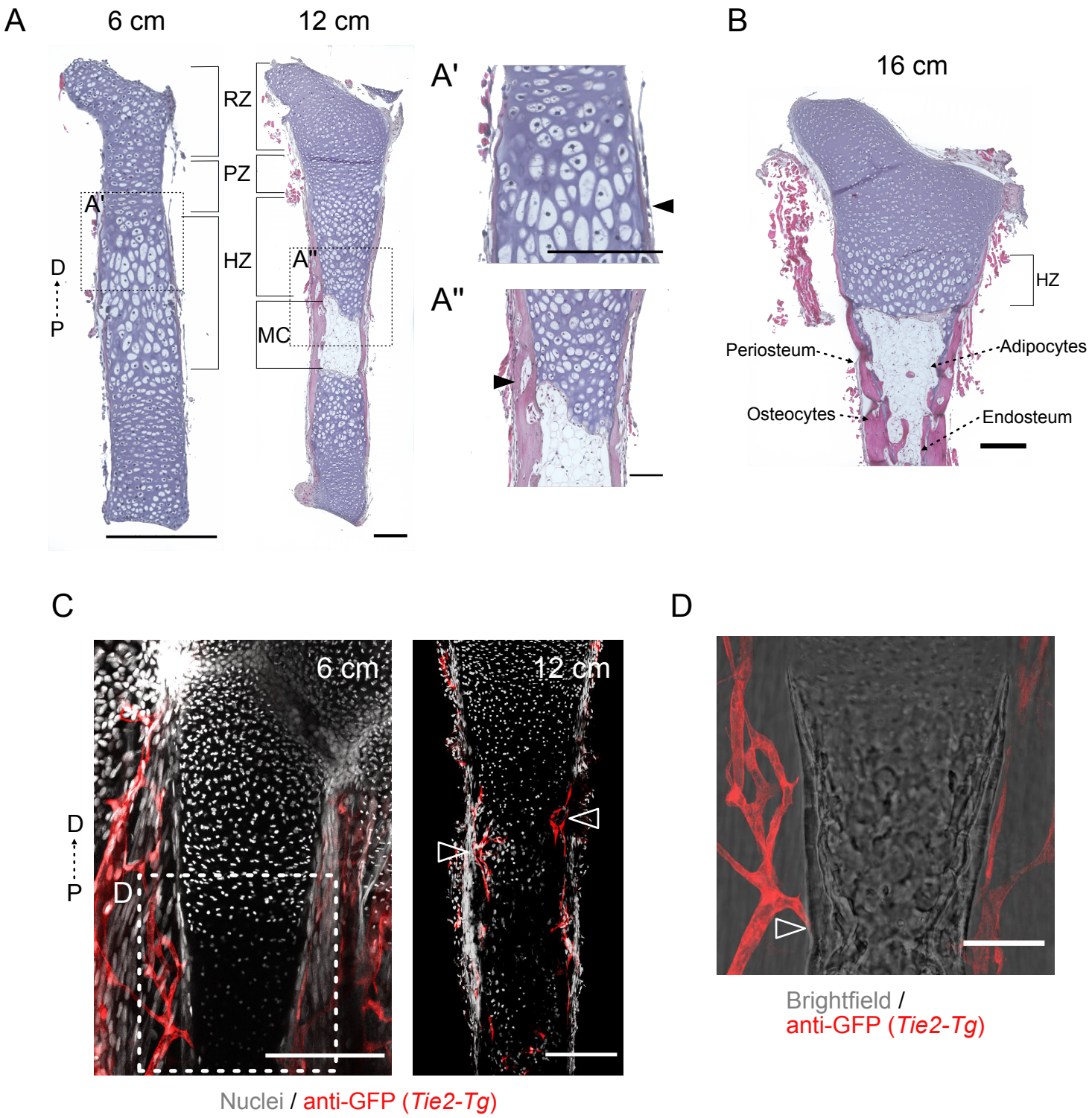
A
6 cm
12 cm
RZ
PZ
HZ
MC
A'
A''
D
P
B
16 cm
HZ
Periosteum
Adipocytes
Osteocytes
Endosteum
C
6 cm
12 cm
D
P
Nuclei / anti-GFP (Tie2-Tg)
D
Brightfield /
anti-GFP (Tie2-Tg)

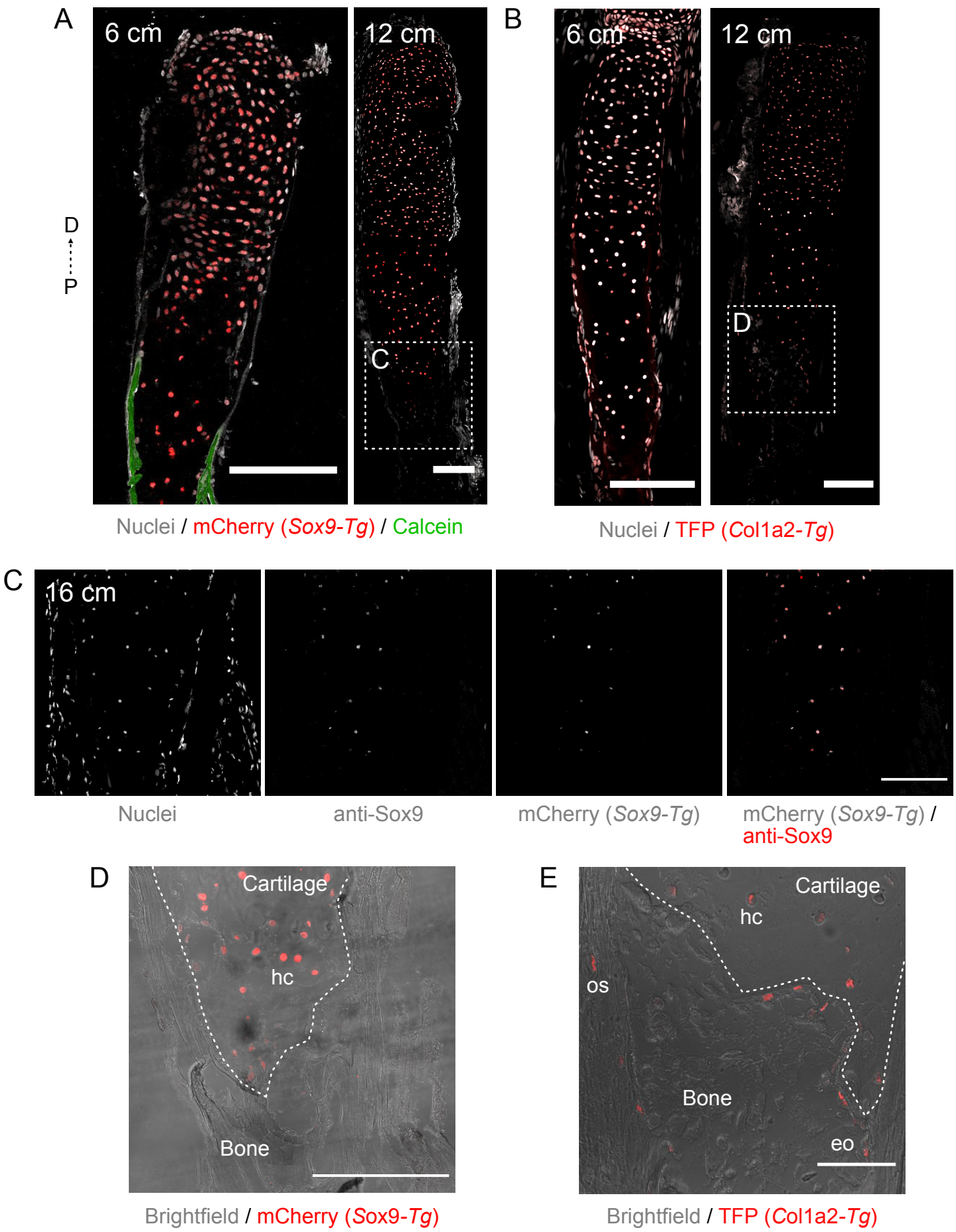
A
6 cm
12 cm
D
P
C
Nuclei / mCherry (Sox9-Tg) / Calcein
B
6 cm
12 cm
D
Nuclei / TFP (Col1a2-Tg)
C
16 cm
Nuclei
anti-Sox9
mCherry (Sox9-Tg)
mCherry (Sox9-Tg) / anti-Sox9
D
Cartilage
hc
Bone
Brightfield / mCherry (Sox9-Tg)
E
Cartilage
hc
os
Bone
eo
Brightfield / TFP (Col1a2-Tg)

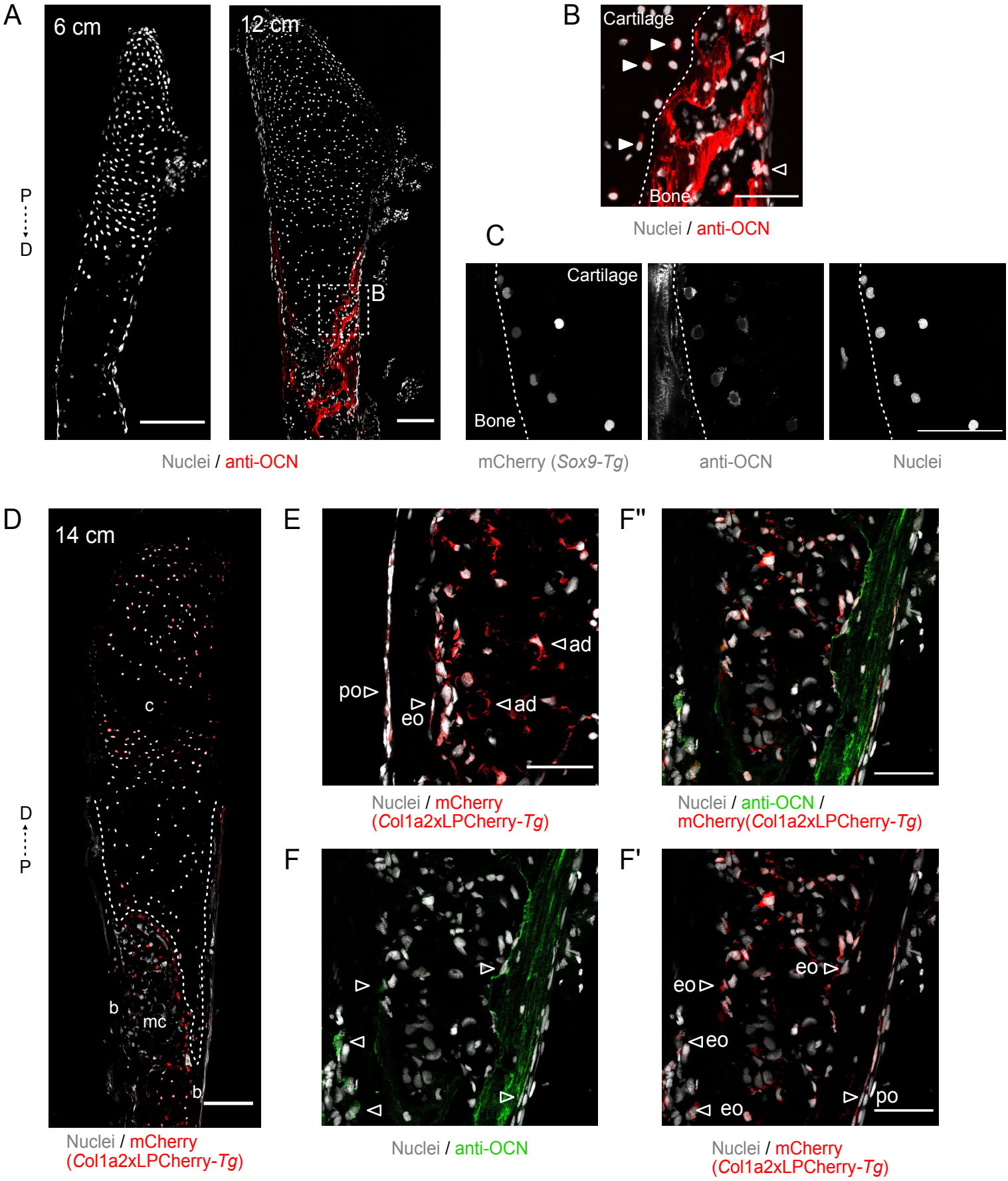
A
6 cm
12 cm
P
D
B
Nuclei / anti-OCN
B
Cartilage
Bone
Nuclei / anti-OCN
C
Cartilage
Bone
mCherry (Sox9-Tg)
anti-OCN
Nuclei
D
14 cm
c
b
mc
b
D
P
Nuclei / mCherry
(Col1a2xLPCherry-Tg)
E
ad
po
eo
ad
Nuclei / mCherry
(Col1a2xLPCherry-Tg)
F"
Nuclei / anti-OCN /
mCherry(Col1a2xLPCherry-Tg)
F
Nuclei / anti-OCN
F'
eo
eo
eo
eo
po
Nuclei / mCherry
(Col1a2xLPCherry-Tg)

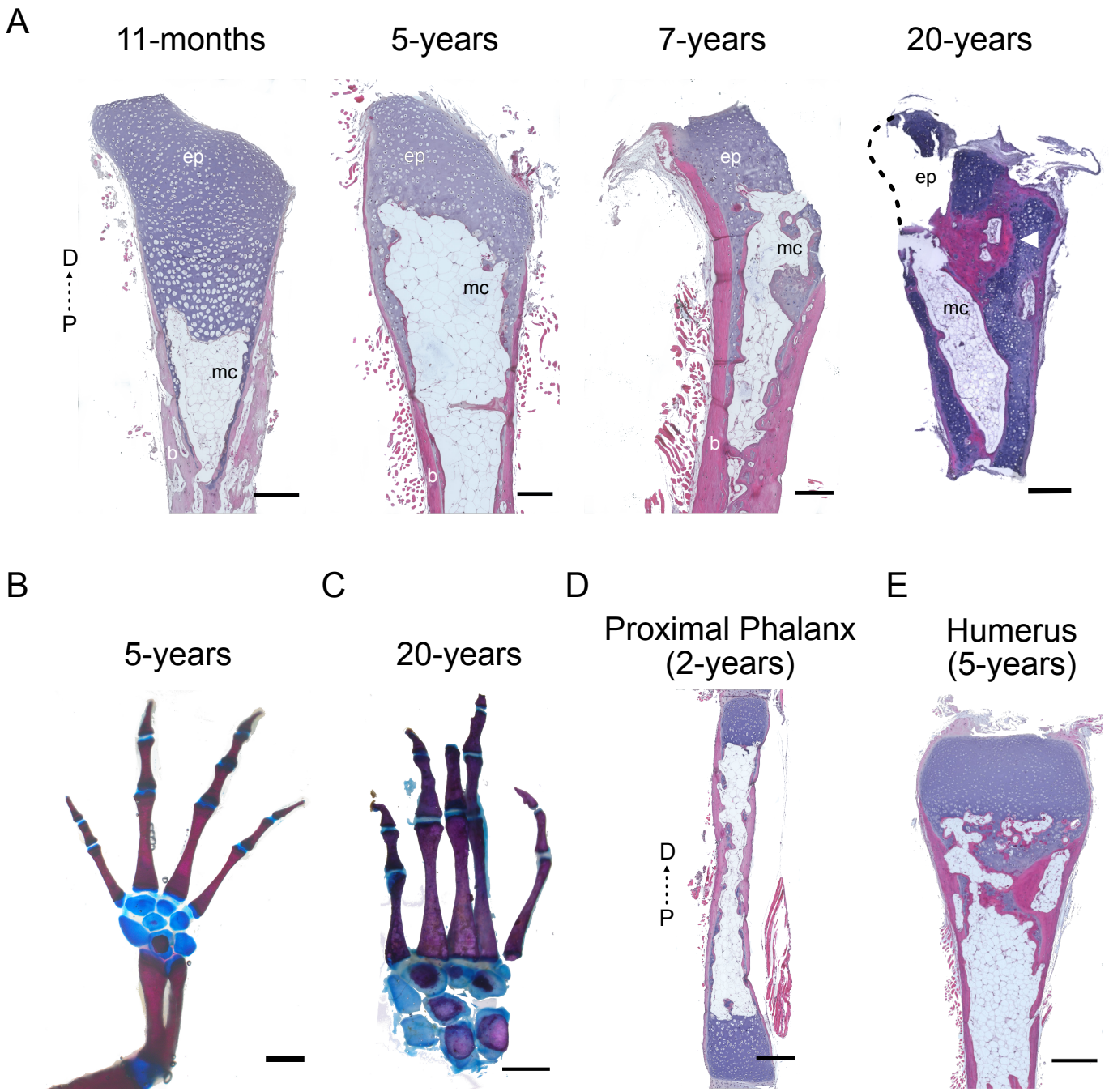
A
11-months
5-years
7-years
20-years
ep
mc
b
D
P
B
5-years
C
20-years
D
Proximal Phalanx
(2-years)
E
Humerus
(5-years)

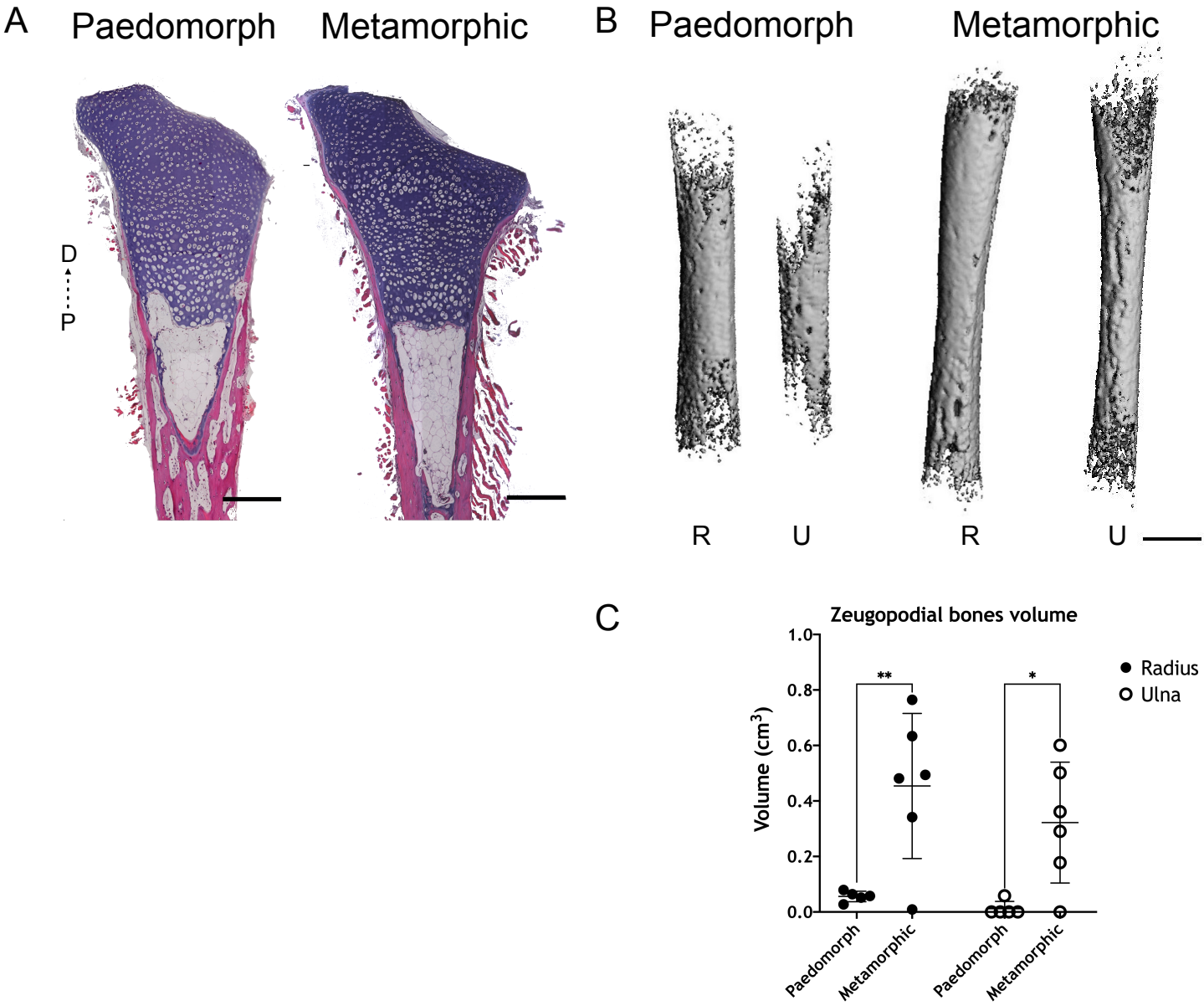
A
Paedomorph
Metamorphic
D
P
B
Paedomorph
Metamorphic
R
U
R
U
C
Zeugopodial bones volume
Volume (cm3)
1.0
0.8
0.6
0.4
0.2
0.0
**
*
Radius
Ulna
Paedomorph
Metamorphic
Paedomorph
Metamorphic